

Two Essential Light Chains Regulate the MyoA Lever Arm To Promote *Toxoplasma* Gliding Motility

Melanie J. Williams,^{a,b} Hernan Alonso,^{a,b} Marta Enciso,^c Saskia Egarter,^{d*} Lilach Sheiner,^{d,e} Markus Meissner,^d Boris Striepen,^e Brian J. Smith,^c Christopher J. Tonkin^{a,b}

The Walter and Eliza Hall Institute, Melbourne, Victoria, Australia^a; Department of Medical Biology, The University of Melbourne, Melbourne, Victoria, Australia^b; La Trobe Institute for Molecular Science, La Trobe University, Melbourne, Victoria, Australia^c; Wellcome Trust Centre for Molecular Parasitology, University Of Glasgow, Glasgow, Scotland, United Kingdom^d; Centre for Tropical and Emerging Global Diseases, University of Georgia, Athens, Georgia, USA^e

* Present address: Saskia Egarter, Parasitology, Department of Infectious Diseases, University of Heidelberg Medical School, Heidelberg, Germany.

ABSTRACT Key to the virulence of apicomplexan parasites is their ability to move through tissue and to invade and egress from host cells. Apicomplexan motility requires the activity of the glideosome, a multicomponent molecular motor composed of a type XIV myosin, MyoA. Here we identify a novel glideosome component, essential light chain 2 (ELC2), and functionally characterize the two essential light chains (ELC1 and ELC2) of MyoA in *Toxoplasma*. We show that these proteins are functionally redundant but are important for invasion, egress, and motility. Molecular simulations of the MyoA lever arm identify a role for Ca²⁺ in promoting intermolecular contacts between the ELCs and the adjacent MLC1 light chain to stabilize this domain. Using point mutations predicted to ablate either the interaction with Ca²⁺ or the interface between the two light chains, we demonstrate their contribution to the quality, displacement, and speed of gliding *Toxoplasma* parasites. Our work therefore delineates the importance of the MyoA lever arm and highlights a mechanism by which this domain could be stabilized in order to promote invasion, egress, and gliding motility in apicomplexan parasites.

IMPORTANCE Tissue dissemination and host cell invasion by apicomplexan parasites such as *Toxoplasma* are pivotal to their pathogenesis. Central to these processes is gliding motility, which is driven by an actomyosin motor, the MyoA glideosome. Others have demonstrated the importance of the MyoA glideosome for parasite motility and virulence in mice. Disruption of its function may therefore have therapeutic potential, and yet a deeper mechanistic understanding of how it works is required. Ca²⁺-dependent and -independent phosphorylation and the direct binding of Ca²⁺ to the essential light chain have been implicated in the regulation of MyoA activity. Here we identify a second essential light chain of MyoA and demonstrate the importance of both to *Toxoplasma* motility. We also investigate the role of Ca²⁺ and the MyoA regulatory site in parasite motility and identify a potential mechanism whereby binding of a divalent cation to the essential light chains could stabilize the myosin to allow productive movement.

Received 27 May 2015 Accepted 18 August 2015 Published 15 September 2015

Citation Williams MJ, Alonso H, Enciso M, Egarter S, Sheiner L, Meissner M, Striepen B, Smith BJ, Tonkin CJ. 2015. Two essential light chains regulate the MyoA lever arm to promote *Toxoplasma* gliding motility. *mBio* 6(5):e00845-15. doi:10.1128/mBio.00845-15.

Editor Louis M. Weiss, Albert Einstein College of Medicine

Copyright © 2015 Williams et al. This is an open-access article distributed under the terms of the [Creative Commons Attribution-Noncommercial-ShareAlike 3.0 Unported license](https://creativecommons.org/licenses/by-nc-sa/4.0/), which permits unrestricted noncommercial use, distribution, and reproduction in any medium, provided the original author and source are credited.

Address correspondence to Christopher J. Tonkin, tonkin@wehi.edu.au.

The phylum *Apicomplexa* comprises a group of obligate intracellular parasites, which include medically and agriculturally important pathogens such as *Plasmodium* spp., the causative agents to malaria, *Cryptosporidium* spp., agents of severe gastrointestinal disease, and *Toxoplasma gondii*, the cause of toxoplasmosis. Infection by *Plasmodium* spp. caused an estimated 198 million cases of malaria in 2013, resulting in ~564,000 deaths (WHO World Malaria Report, 2014). *Toxoplasma* parasites, on the other hand, are among the most ubiquitous pathogens of humans, chronically infecting 30% to 80% of populations and causing a range of medical conditions, including acute tissue damage in immunocompromised individuals, congenital birth defects afflicting ~190,000 births per year (1), and progressive blindness in some countries.

As with all apicomplexan species, the virulence of *Toxoplasma*

relies on the ability to perform a unique form of cellular locomotion termed “gliding motility.” Gliding motility is used to traverse host tissue and to invade and, ultimately, egress host cells. It is the destruction of host tissues endured during this cycle that is the predominant cause of disease manifestation by apicomplexan species. Apicomplexan gliding motility is initiated in response to Ca²⁺ signaling events and is accomplished through the generation of mechanical force by an actomyosin motor, termed the glideosome. The glideosome is a multiprotein complex that resides at the parasite pellicle, confined to the space between the plasma membrane (PM) and the inner membrane complex (IMC). The current model suggests that the glideosome comprises a unique type XIV myosin, termed MyoA, anchored to a scaffolding complex made up of the glideosome-associated proteins (GAPs) (2–4). The glideosome is anchored to the IMC by transmembrane

proteins GAP40 and GAP50 and members of the GAPM family (3, 5, 6), while GAP45 acts as a molecular tether between the IMC and the PM, maintaining a critical distance between the two membrane systems (3). MyoA then attaches to the GAP complex courtesy of a unique N-terminal extension on its regulatory light chain (RLC), MLC1 (*Plasmodium* myosin A tail-interacting protein [MTIP] homologue) (3, 7, 8). In order to move with respect to the host environment, transmembrane adhesins displayed on the surface of parasites are thought to link to the glideosome through their short cytoplasmic tails. Previous evidence suggested that the glycolytic enzyme aldolase may act as a bridge between the cytoplasmic tails of adhesins and the actin filaments (9, 10) and allowed the proposal of a model that suggested that MyoA activity and actin treadmill drag transmembrane adhesins through the plasma membrane rearward, which in turn drives forward parasite motion. Recent evidence, however, suggests that aldolase is likely not an actin-adhesin bridging protein and there may be some differences between the motor that drives invasion and that which drives tissue dissemination and that this linear model is an oversimplification of how the glideosome functions (11–13).

Despite this basic molecular understanding of motility, the mechanisms that regulate the activity of MyoA and how this complex generates force remain largely unknown. In other systems, myosins are usually made up of head, neck, and tail domains. The head domain hydrolyzes ATP, amplifying small changes in the active pocket, which leads to a large conformational change in the converter domain, allowing pivoting against the lever arm. The myosin lever arm consists of the myosin neck region in association with regulatory light chains (analogous to *Toxoplasma* MLC1), essential light chains (ELCs), or calmodulins (CaM). The lever arm is also often a regulatory site, where direct interactions with Ca^{2+} or with Ca^{2+} -dependent phosphorylation events can modulate motor activity (14–18). While MyoA has been shown to be a fast, single-headed plus-end-directed motor (7), little evidence exists on how this unique myosin is activated by the signaling events that are known to regulate motility. MyoA and MLC1 have been shown to be phosphorylated upon activation of motility (19–21), and yet subsequent functional studies demonstrated that this posttranslational modification has little to no role in its activation (22, 23). Furthermore, until recently, only a single light chain—MLC1—was known to exist, thus limiting the possibilities for investigating motor regulation by the lever arm.

Here we identify a novel essential light chain (ELC2) and describe the function of this and the previously identified ELC1 of *Toxoplasma* MyoA, thus defining the full lever arm of this important molecular motor. We show that ELC1 binds Ca^{2+} and use structural modeling and molecular dynamics in combination with functional studies to show that key residues predicted to coordinate an interaction interface between ELC1 and MLC1, mediated by Ca^{2+} , can affect the quality, speed, and displacement of parasites as they move across a substrate. Our work therefore provides the first insight into how the MyoA lever arm is stabilized in order to provide structural rigidity for force generation during the motility of apicomplexan parasites.

RESULTS

***Toxoplasma* ELC2 associates with the glideosome.** Previously, we identified a potential essential light chain (ELC1) of the *Toxoplasma* glideosome using quantitative proteomic techniques (19). Upon further interrogation of the remaining hypothetical pro-

teins detected in the same experiment, we identified a second calmodulin-like protein (TGME49_305050) with a predicted mass of 15 kDa, four putative EF hands (EFs) (Ca^{2+} binding regions), and 68% protein sequence similarity to ELC1. The striking similarities suggested to us that TGME49_305050 may be a second essential light chain (ELC2) and prompted us to investigate its potential association with the glideosome.

To determine the localization and potential interaction of ELC2 with the glideosome, we genetically fused a triple-hemagglutinin (HA₃) epitope tag to the C terminus of this protein at the endogenous locus and performed immunofluorescence and coimmunoprecipitation (Co-IP)-Western blot analyses of ELC2-HA-expressing parasites (Fig. 1). Expression of ELC2-HA was confirmed by Western blotting and compared to expression of parental (RHΔHX) and ELC1-HA-expressing parasites (Fig. 1A) (19). Probing with anti-HA antibodies detected a protein of ~18 kDa in ELC2-HA lysate comparable to ELC1-HA at 17 kDa, whereas nothing was detected in the parental control (Fig. 1A, left panel). Antibodies raised to recombinant ELC1 revealed a single 15-kDa protein in parental and ELC2-HA-expressing parasites but only a higher band (17 kDa), corresponding to the HA-tagged version of ELC1, in ELC1-HA parasites, thus confirming that anti-ELC1 antibodies do not cross-react with ELC2 (Fig. 1A, right panel). Immunofluorescence microscopy of intracellular parasites expressing ELC2-HA showed that this protein resides at the parasite periphery and colocalizes with staining by anti-GAP45 antibodies (Fig. 1B, bottom panel). The localization observed was very similar to that observed from parasites expressing ELC1-HA (Fig. 1B, top panel) and was thus consistent with ELC2 being a component of the glideosome. We then performed Co-IP of ELC2-HA lysate with anti-HA to formally establish the interaction of this protein with various components of the *Toxoplasma* glideosome. Upon probing of IP eluates of parental, ELC1-HA (positive control), and ELC2-HA parasites with antibodies against the MyoA glideosome, we determined that ELC2 specifically interacts with glideosome components MyoA, GAP45, and MLC1 (Fig. 1C). Interestingly, antibodies to ELC1 did not detect a signal from the ELC2-HA IP, demonstrating that ELC1 and ELC2 (ELC1/2) do not exist within the same glideosome complexes and therefore likely compete for the same binding site (Fig. 1C). To further demonstrate the specificity of the interaction between ELC2 and the glideosome, we performed a reciprocal IP with anti-GAP45 antibodies and demonstrated that ELC1-HA and ELC2-HA were copurified but that they were not copurified when normal rabbit (nonspecific) serum (NS) was used (Fig. 1D). Taken together, these results show that ELC2 is a novel component of the *Toxoplasma* MyoA glideosome which interacts in a mutually exclusive manner with ELC1.

ELC1 and ELC2 interact with the MyoA neck and, together with MLC1, define the lever arm. The interaction of an essential light chain with its myosin heavy chain occurs at the myosin neck. The complex that they form, together with other regulatory light chains (analogous to *Toxoplasma* MLC1) or CaM proteins, defines the myosin lever arm, which forms a stable structure for the myosin head to pivot against to create force (24). Recently, Bookwalter et al. showed that ELC1 forms a complex with MyoA upon coexpression using the baculovirus/Sf9 insect cell expression system and that this interaction increased the speed at which MyoA moved actin filaments (25). To specifically determine if ELC1 and ELC2 interact with the neck of MyoA, we first defined this region

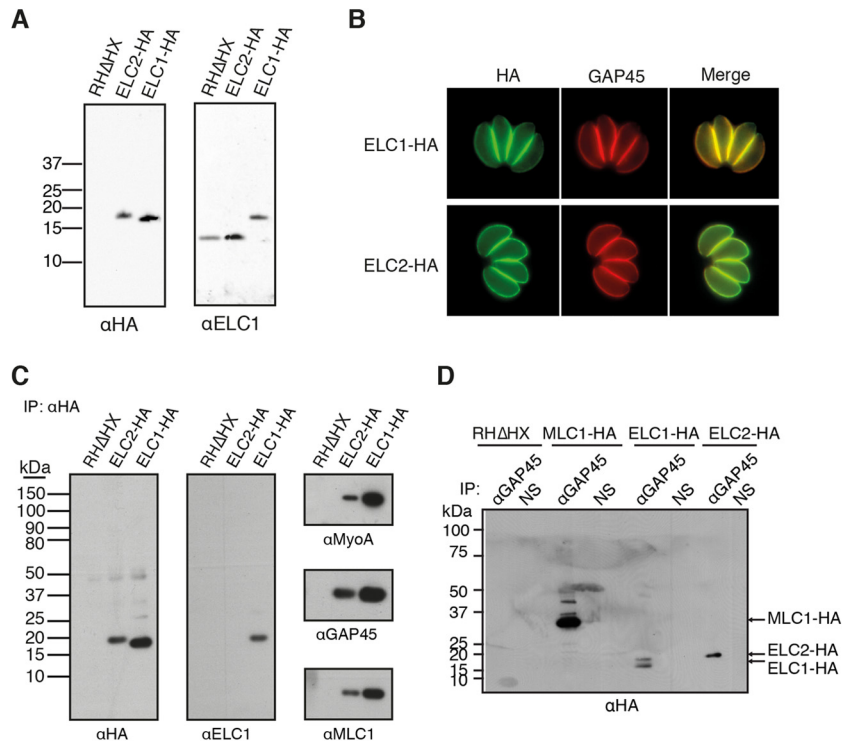


FIG 1 ELC2 is a novel component of the MyoA glideosome. (A) Western blot analysis of lysate from ELC2-HA, ELC1-HA, and parental (RH Δ HX) parasites probed with mouse monoclonal anti-HA antibodies (left panel) and rabbit polyclonal anti-ELC1 antibodies (right panel). (B) Immunofluorescence analysis of intracellular parasites expressing ELC1-HA and ELC2-HA with anti-HA antibodies (green). The pellicle was detected by costaining with anti-GAP45 antibodies (red). (C) Immunoprecipitation (IP) of lysate from parental parasites or parasites expressing ELC1-HA or ELC2-HA with mouse monoclonal anti-HA antibodies. Eluates were analyzed by Western blotting with rabbit anti-HA antibodies (left panel) and with anti-GAP45, anti-MyoA, anti-MLC1 (right panels), and anti-ELC1 (middle panel). (D) Co-IP of the same lysate as that described for panel C with anti-GAP45 antibodies and nonspecific serum (NS) as a negative control. Eluates were analyzed by Western blotting with anti-HA antibodies.

to be the last 61 amino acids of MyoA (amino acids 770 to 831), where residues 770 to 799 and 800 to 831 contained the putative ELC and MLC1 binding sites, respectively (Fig. 2A). To investigate this we generated transgenic versions of the MyoA neck fused to the FKBP-derived destabilization domain (DD) (26) and an Ty epitope tag (27) for the full neck region (DDTyMyoA_{770–831}) or a truncation lacking the putative ELC binding region (DDTyMyoA_{800–831}) (Fig. 2B). These constructs were transiently introduced into Δ MyoA *Toxoplasma* parasites (13) and analyzed for size by Western blotting with anti-Ty antibodies. The bands were predicted to be ~20 kDa (DDTyMyoA_{770–831}) and ~16.5 kDa (DDTyMyoA_{800–831}) but ran higher (~25 kDa and 20 kDa, respectively), likely due to hydrophobicity. The localizations of ELC1, MLC1, and GAP45 were examined by immunofluorescence microscopy (Fig. 2D). Consistent with our model, and in agreement with previous data (13), the absence of MyoA had no effect on the targeting of GAP45 or MLC1 to the pellicle. However, peripheral localization of ELC1 was lost and replaced with speckled, cytosolic staining, confirming that MyoA is required to target this CaM-like protein to the parasite periphery (Fig. 2D, upper panel). Expression of the full MyoA neck (DDTyMyoA_{770–831}) rescued the localization of ELC1 (Fig. 2D, middle panel), but expression of a truncated MyoA neck lacking the predicted ELC binding site (DDTyMyoA_{800–831}) did not (Fig. 2D, bottom panel).

To confirm these findings, we then heterologously expressed ELC1, ELC2, and the MyoA neck region in *Escherichia coli* and

tested their capacity to interact *in vitro* by gel filtration chromatography (Fig. 2E). A shift in the retention time was observed for both ELC1 and ELC2 preincubated with MyoA_{770–831} compared to the results seen with the individual components alone (Fig. 2E, panels i and ii). These results suggest that both ELC1 and ELC2 interact specifically with the MyoA neck, requiring the residues between 770 and 799 and thus defining the lever arm of the MyoA glideosome. Furthermore, this also indicates that ELC1 and ELC2 bind to the same region of MyoA.

The IQ motif is a highly basic sequence of approximately 23 amino acids, with a conserved core that usually fits the consensus sequence IQXXRGXXR/K. A very degenerate IQ motif is present downstream from the MLC1 binding site (Fig. 2A). Refinement of the structural model presented previously (19) using molecular dynamics favors interaction of ELC1 with residues 782 to 792 (LVSVLEAYYAG) of MyoA (Fig. 2F). To test this prediction, a full-length His-StrepII-Flag (HSF)-tagged copy of MyoA (HSF-MyoA) was complemented into Δ MyoA parasites (13) and 3 key hydrophobic residues (L782, L786, and Y790) within the predicted ELC binding site were mutated to alanine to create HSF-MyoA-LLY/AAA (Fig. 2G). Widefield fluorescence microscopy was performed on Δ MyoA parasites that were complemented with wild-type HSF-MyoA or mutant HSF-MyoA-LLY/AAA. While staining with anti-Flag showed peripheral localization for both wild-type MyoA and mutant MyoA, anti-ELC1 antibodies detected peripheral staining in wild-type-complemented parasites

only and speckled cytosolic staining in mutant-complemented parasites (Fig. 2H), suggesting that the 3 hydrophobic residues tested are important for ELC1 binding. Despite several attempts, parasites stably expressing HSF-MyoA-LLY/AAA could not be isolated for testing of the functional significance of disrupting this interaction. It is worth noting that removal of MyoA or disruption of the interaction between MyoA and ELC1 led to a speckled rather than diffuse distribution of ELC1 (Fig. 2D, top and bottom panels). The possibility cannot be ruled out that disruption of its interaction with MyoA may cause misfolding of ELC1 and, consequently, mislocalization to inclusion bodies; however, the *in vitro* data support the conclusion of the presence of a specific interaction between the MyoA neck and ELC1.

A single essential light chain (ELC1 or ELC2) is required for efficient *Toxoplasma* invasion and egress. To determine the importance of ELC1 and ELC2, conditional knockout (cKO) lines were generated by replacing the endogenous promoter of ELC1 or ELC2 with an anhydrotetracycline (ATc)-regulatable promoter in the Δ Ku80:TATi strain (28, 29) (Fig. 3A, panel i). In addition, N-terminal triple-HA tags were inserted, creating the cKO-HA₃-ELC1 and cKO-HA₃-ELC2 parasite lines (referred to here as cKO-ELC1 and cKO-ELC2). Regulation of the loci was assayed by growing parasites for 48 or 96 h in the presence of 1.0 μ g/ml ATc. Western blot analysis performed with anti-HA demonstrated the progressive loss of ELC expression in both cKO-ELC1 and cKO-ELC2 parasites (Fig. 3B). Probing with anti-ELC1 antibodies demonstrated the absence of cross talk in expression of the two light chains, and antibodies to *Toxoplasma* catalase were used as a loading control (Fig. 3B). Wide-field fluorescence microscopy of intracellular cKO-ELC1 and cKO-ELC2 parasites following ATc treatment confirmed the absence of ELC1 and ELC2, respectively (Fig. 3C).

To assess the function of ELC1 and ELC2, we assayed the ability of mutant parasite lines to invade and egress host cells. Following growth for 96 h in the presence of ATc, cKO-ELC1 and cKO-ELC2 parasites invaded and egressed normally compared to untreated and wild-type control parasites (Fig. 3D and E).

To investigate potential functional redundancy of the ELCs, we next used double-crossover homologous recombination to delete ELC1 in the cKO-ELC2 line to derive a conditional double-KO line (cDKO-ELC) (Fig. 3A, panel ii). In contrast to single-cKO lines, ATc treatment of cDKO-ELC parasites reduced their ability to invade host cells to 10% of that of the wild type (Fig. 3D). Furthermore, the capacity of parasites to egress in response to stimulation for 2.5 min with the Ca²⁺ A23187 ionophore was severely attenuated (Fig. 3E). ATc-treated cDKO-ELC parasites were then complemented by transfection with ectopic DDTy-tagged ELC1 or ELC2. Stabilization of DDTyELC1 or DDTyELC2

with Shld-1 fully restored the invasion and egress capabilities of the mutant parasites (Fig. 3D and E), thus highlighting that ELC1 and ELC2 are functionally redundant in their roles as the essential light chain(s) of MyoA during *Toxoplasma* egress and invasion.

ELC1 and ELC2 are required for the stability of MyoA. As a first step to determining the function of ELC1 and ELC2 in the glideosome, we investigated the assembly of the glideosome in their absence. The data presented in Fig. 2D demonstrate that MyoA is required for correct localization of ELC1. We then tested the reciprocal effect of ELC depletion on the assembly and stability of MyoA at the pellicle. To do this, MyoA was N-terminally tagged by double homologous recombination with a His-Flag-StrepII (HFS) tag in cDKO-ELC parasites and the localization of HFS-MyoA was observed after ELC depletion by ATc. Unexpectedly, microscopy of intracellular parasites probed with anti-Flag tag antibodies detected greatly diminished levels of HFS-MyoA after treatment with ATc (Fig. 4A). In contrast, anti-MLC1 antibodies stained MLC1 at the periphery of parasites in both the presence and absence of ELC. Interestingly, a secondary localization of MLC1 was prominent upon suppression of ELC, where an apparent intracellular structure was marked. This mislocalization is possibly a cellular response specific to the absence of ELC. Further investigation by Western blotting showed that depletion of MyoA is concomitant with the depletion of both ELCs but not of either alone (Fig. 4B), suggesting that MyoA stability is tightly coupled to ELC function.

Ca²⁺ interacts with ELC1 and potentially causes an intermolecular interaction between ELC1 and MLC1. To better understand the role of the ELCs in the function of the MyoA lever arm, in the absence of a crystal structure, we turned to structural modeling. Previously, we presented a homology model of the lever arm complex (MyoA neck-ELC1-MLC1) based on the solved structure of the scallop myosin II lever arm complex (19). Here, we extended this model to the complete MyoA protein and performed molecular dynamics for refinement. The MyoA head has a nucleotide-binding pocket, so by inclusion of the full-length MyoA protein we were able to model the complex in various states of its duty cycle. First, ADP was introduced in the nucleotide-binding site and Ca²⁺ included at ELC1 EF hand I (EFI), similarly to that seen with scallop myosin II. The model predicted Ca²⁺ to be coordinated by the side chains of ELC1 residues D15, D17, and D19 (Fig. 5A). The binding affinity of Ca²⁺ was estimated by performing pulling simulations of Ca²⁺ from EFI to calculate the change in free energy (Δ G), which was determined to be 79.0 kJ/mol (data not shown). Furthermore, ELC1 EFI was predicted to interact with MLC1 by backbone hydrogen bonds between ELC1-D17 and MLC1-E179 (Fig. 5A). This interaction between the two light chains was analyzed by molecular dynamics simulations,

Figure Legend Continued

N-terminal DDTy tags. The full MyoA neck sequence is 61 amino acids in length (residues 770 to 831). Truncation of residues 770 to 799 removed the predicted ELC binding site. (C) Western blot analysis of mouse monoclonal anti-Ty antibodies and of lysate from RH Δ HX parasites expressing the transgenes shown in panel B. (D) Immunofluorescence analysis of Δ MyoA parasites transiently expressing DDTyMyoA₇₇₀₋₈₃₁ and DDTyMyoA₈₀₀₋₈₃₁. MyoA transgenes were stabilized by overnight treatment with Shld-1 and detected using mouse anti-Ty antibodies. Localization of glideosome components was detected with rabbit anti-GAP45, anti-MLC1, and anti-ELC1 antibodies. (E) Size exclusion chromatography of recombinant ELC1, ELC2 (blue), and MyoA neck (black) regions either separately or together (red). (F) Homology model of the MyoA lever arm predicting that key residues of the MyoA neck (green) interact with ELC1 (orange). (G) Schematic representation of a transgenic version of MyoA. The full MyoA coding sequence was N-terminally fused to His-Flag-StrepII tags, and three key residues predicted to interact with ELC1 (highlighted in panel F) were mutated to alanine. (H) Immunofluorescence analysis of HFS-MyoA and HFS-MyoA-LLY/AAA expressed transiently in Δ MyoA parasites (13) by the use of mouse monoclonal anti-Flag tag antibodies. The localization of ELC1 was examined using anti-ELC1 antibodies. Bars, 5 μ m.

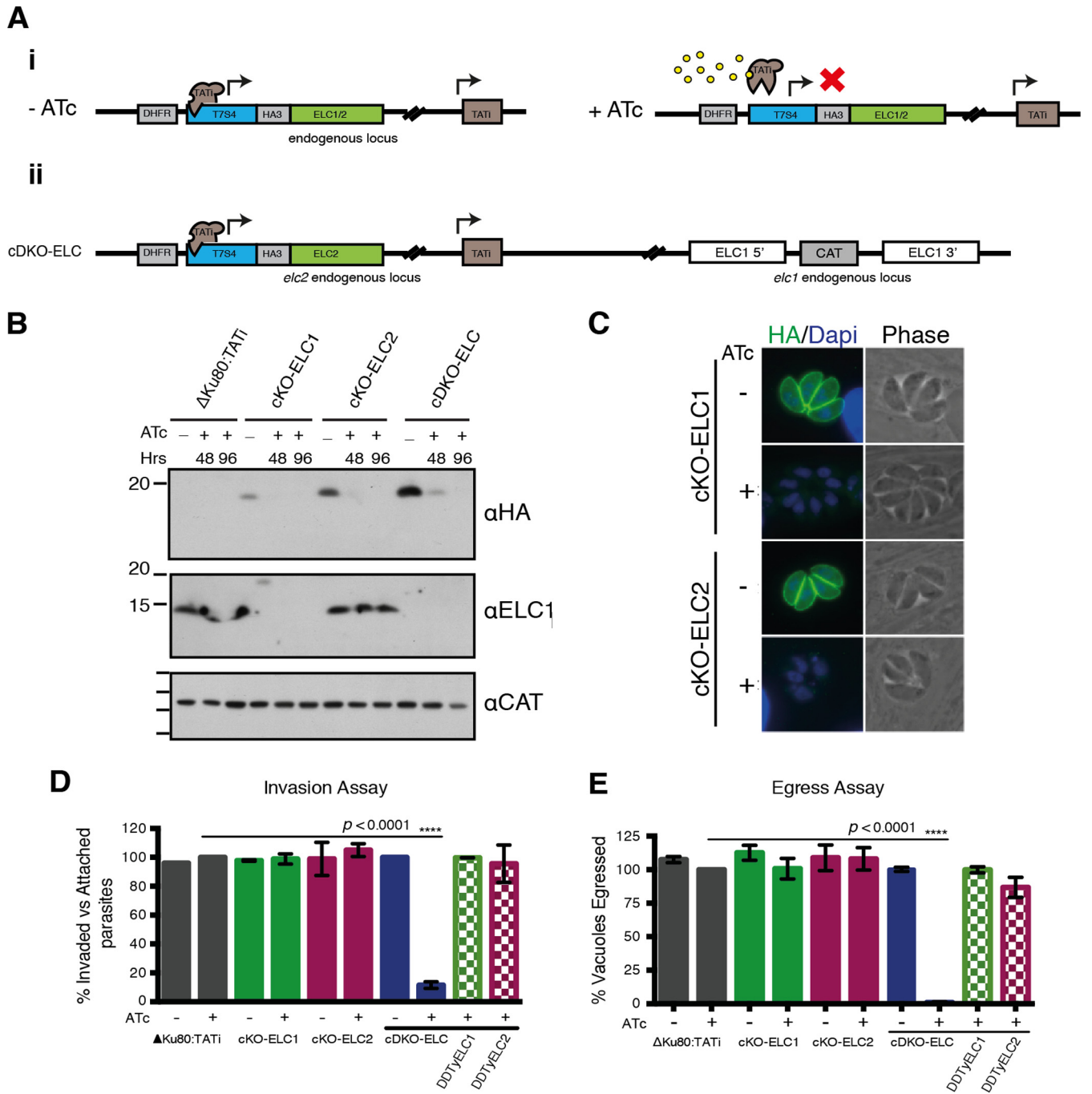


FIG 3 Conditional deletion of ELC1 and ELC2 and simultaneous removal of both essential light chains. (A) Schematic representing the genetic methods used to regulate endogenous essential-light-chain expression. (i) The genetic strategy used to create ELC1 and ELC2 conditional knockouts. The endogenous promoter of ELC1 and ELC2 was replaced with 7 Tet operating sequences and the SAG4 minimal promoter (T7S4) in Δ Ku80:TATi parasites (29). A HA₃ epitope tag was inserted at the N terminus of ELC1 and ELC2, and transformants were selected for the *dhfr* gene. In the presence of anhydrotetracycline (ATc), the Tet transactivator (TATi) drives transcription of ELC1/2. In the presence of ATc, transcription is switched off. (ii) The genetic strategy used to create ELC1 and ELC2 double-knockout parasites. The *elc1* ORF was replaced with *cat* to confer chloramphenicol resistance in cKO-ELC2 parasites. (B) Western blot analysis of lysate from Δ Ku80:TATi, cKO-ELC1, cKO-ELC2, and cDKO-ELC parasites following treatment with 1.0 μ g/ml ATc. Lysates were probed with mouse anti-HA, rabbit anti-ELC1, and anti-catalase as a loading control. (C) Immunofluorescence analysis of intracellular cKO-ELC1 and cKO-ELC2 parasites grown in the presence and absence of 1.0 μ g/ml ATc for 96 h. DAPI, 4',6-diamidino-2-phenylindole. (D) Two-color invasion assay performed on parasites grown with or without ATc for 96 h. DDTy-ELC1 and DDTy-ELC2 expression was stabilized by 1.0 μ M Shld-1 at ~10 h prior to invasion. Numbers of invaded and total parasites were counted from >5 fields per slide. (E) Fixed-egress assay performed on intracellular vacuoles grown for 30 h prior to stimulation with 8 μ M A23187. More than 100 vacuoles were counted for each slide. In panels D and E, duplicate or triplicate slides were counted per experiment. Column data represent mean percentage results from 3 independent experiments. Error bars represent \pm SEM.

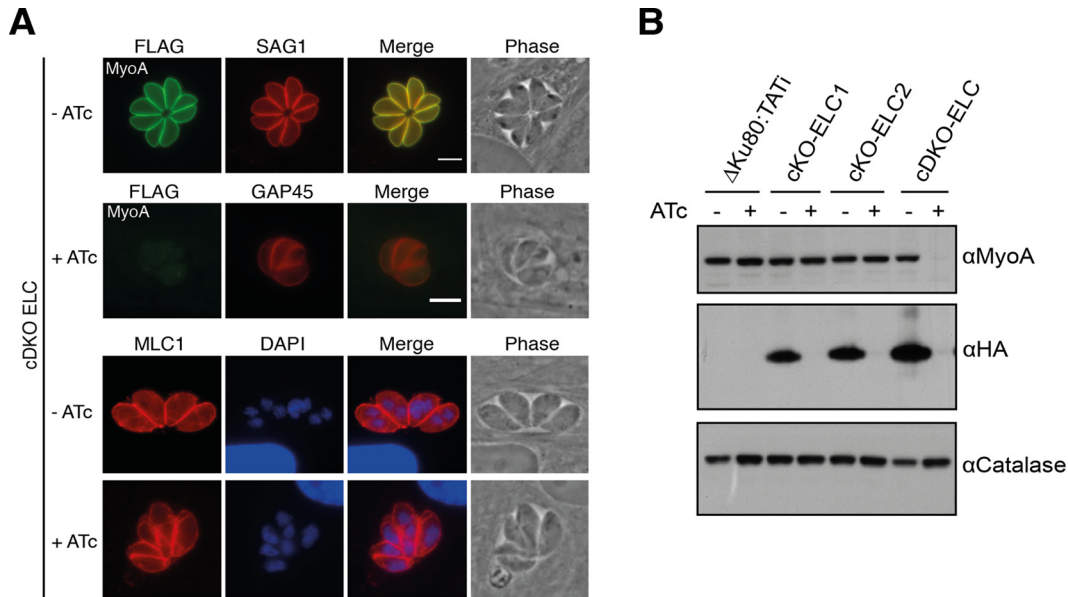


FIG 4 Assembly of the MyoA glideosome is disrupted in the absence of two essential light chains. (A) Immunofluorescence analysis of cDKO-ELC parasites grown with or without ATc. MyoA was detected using anti-Flag in parasites expressing His-Flag-StrepII-MyoA, and the pellicle was marked using anti-GAP45 antibodies. Expression of MLC1 was detected using anti-MLC1 antibodies. Bars, 5 μ m. (B) Western blot analysis of Δ Ku80:TATI, cKO-ELC1, cKO-ELC2, and cDKO-ELC parasites grown in the absence or presence of ATc for 7 days and probed with anti-MyoA, anti-HA, and anti-catalase.

and, interestingly, it was only in simulations when Ca^{2+} was included at EFI that a stable interaction formed between the two light chains, as measured by the distance between the interacting residues (Fig. 5B; see also Video S1 and Video S2 in the supplemental material). The functional redundancy between ELC1 and ELC2 suggests that key features and residues that contribute to their role in the MyoA lever arm are likely conserved. To investigate the molecular basis for redundancy, we also generated a structural model in which ELC1 was replaced with ELC2 (Fig. 5C). Residues D15 and D19 are conserved between the two essential light chains (ELC2 residues D16 and D20). The only difference around the Ca^{2+} binding pocket is found in residue 17/18, which is an aspartate in ELC1 and an asparagine in ELC2. This does not imply a large difference regarding the Ca^{2+} binding. The interaction between ELC1/2 and MLC1 is not affected either, as it is mediated by backbone interactions (Fig. 5A). Furthermore, when ADP was replaced by ATP at the nucleotide-binding site, a large conformational change, driven by the bending of the MyoA lever arm (see Fig. 5D in comparison to 5A [green]), changed the relative orientations of the two light chains, and both ELC1-R8 and ELC2-R9 moved into close proximity to the MLC1 backbone (Fig. 5D).

To test these predictions *in vitro*, we cloned ELC1 into an *E. coli* expression vector and introduced several different mutations to assess their effect on Ca^{2+} binding. We chose to mutate D15 to alanine, as this mutation was predicted to ablate Ca^{2+} binding at EFI (data not shown). To assess the ELC1-MLC1 interaction in the MyoA-ATP state, we mutated ELC1 R8 to alanine, which was predicted to disrupt the interaction but not affect Ca^{2+} binding to EFI. Mutant versions of ELC1 were then expressed and purified from *E. coli* in the same manner as with the wild type.

The interaction of ELC1 and Ca^{2+} was studied using a thermal shift assay. Sypro-Orange fluorescent dye emits fluorescence upon binding hydrophobic regions. Therefore, as the hydrophobic re-

gions of proteins are exposed when the temperature is increased and the proteins denature, the level of fluorescence emitted also increases. A thermal denaturation curve is obtained by measuring absorbance over time. Because the thermal stability of a protein changes upon binding of an ion such as Ca^{2+} , this assay was able to detect a potential interaction between ELC1 and Ca^{2+} by comparing the effects of temperature on absorbance in the presence of either EGTA or Ca^{2+} . We performed thermal shift assays on wild-type ELC1 and on R8A and D15A mutants in the presence of either Ca^{2+} or EGTA (Fig. 5E, panels i to iii). As predicted, a shift in the thermal denaturation curve of ELC1 was seen in the presence of Ca^{2+} compared to EGTA, indicating that an interaction occurred (Fig. 5E, panel i). Similarly, a shift between curves when ELC1-R8A was tested showed that this mutation did not affect Ca^{2+} binding (Fig. 5E, panel iii). In contrast, little to no change in the curve was observed for the ELC1-D15A mutant, suggesting that this mutation was sufficient to disrupt Ca^{2+} binding and therefore that EFI is likely the only functional Ca^{2+} binding site on recombinant ELC1 (Fig. 5E, panel ii). We next determined the affinities of ELC1 and R8A for Ca^{2+} to be $37 (\pm 9) \mu\text{M}$ and $43 (\pm 10) \mu\text{M}$, respectively, further suggesting that the R8A mutation did not affect Ca^{2+} binding (Fig. 5F, panels i and ii).

Molecular dissection of predicted MyoA lever arm interactions during *Toxoplasma* infectivity. Given our modeling and *in vitro* data described above, we hypothesized that Ca^{2+} binding to ELC1/2 and the subsequent interaction between ELC1/2 and MLC1 that our modeling data predicted would stabilize the MyoA lever arm to provide a rigid structure against which the head domain could pivot to perform a power stroke for productive *Toxoplasma* invasion, egress, and motility. In order to investigate this functionally, we created point mutations in either ELC1 or MLC1 and used these to complement conditional KO strains (Fig. 6). We stably transfected cDKO-ELC parasites with an ectopic version of wild-type ELC1 (DDTy-ELC1) and mutant form R8A or D15A

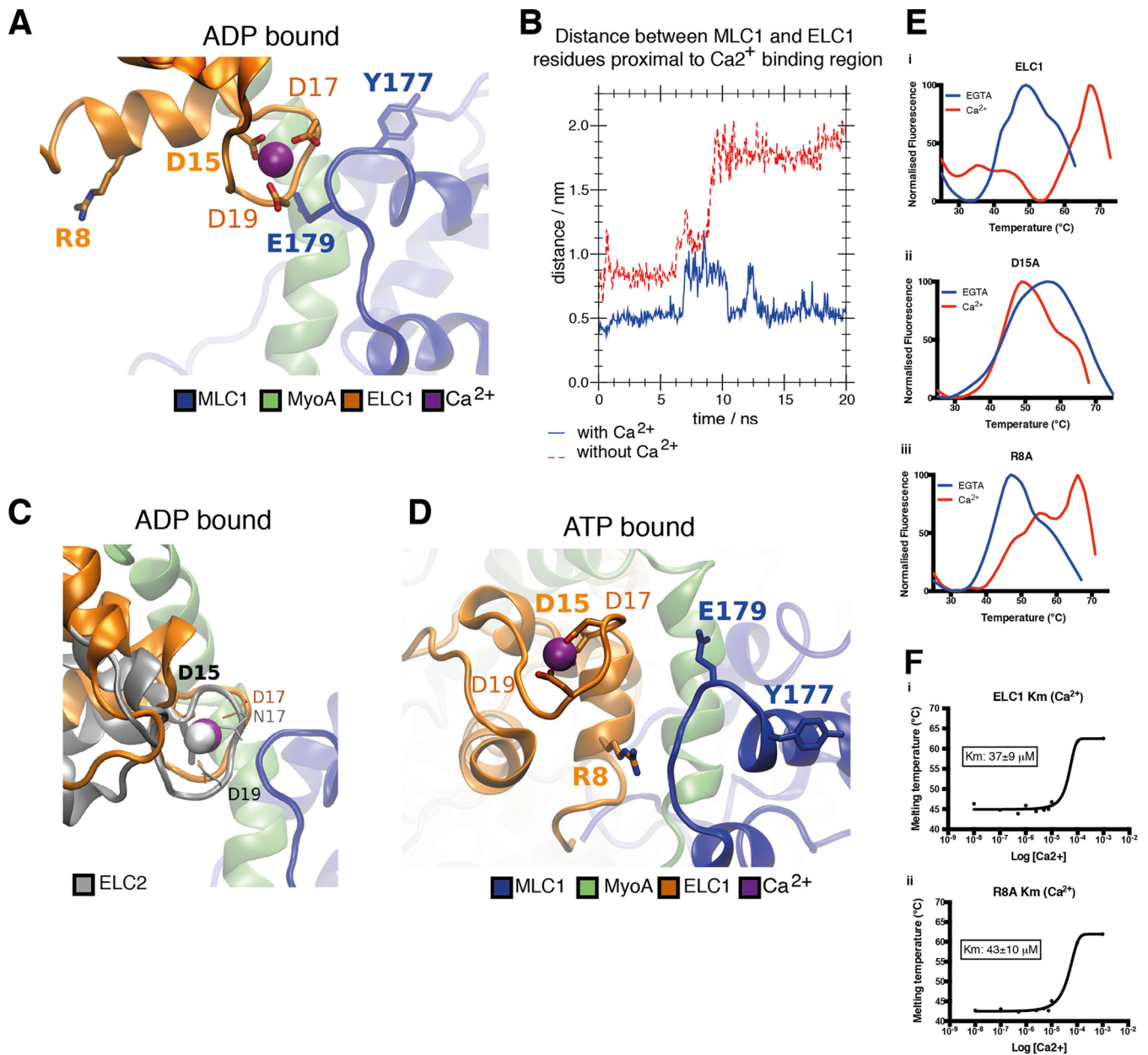


FIG 5 Ca²⁺ binds to ELC1 at EFI, and homology modeling predicts key interactions important for essential-light-chain function. (A) Structural model of MyoA, ELC1, and MLC1 based on the crystal structures of scallop myosin, with ADP simulated at the nucleotide-binding site of MyoA. A predicted interaction with Ca²⁺ is shown at EFI, coordinated by the side chains of ELC1 residues. Potential backbone interactions exist between ELC1 D17 and the side chain of MLC1 E179. (B) The interaction between ELC1 and MLC1 is Ca²⁺ dependent. The distances between the interacting residues shown in panel A were measured during simulations performed in the presence and absence of Ca²⁺. (C) A structural model of MyoA, MLC1, and ELC2 superimposed on the model shown in panel A. (D) The ATP-bound state of the homology model shown in panel A shows a conformational change of ELC1 EFI. (E) Thermal shift assays on recombinant wild-type ELC1 (i) and mutant ELC1 (ii and iii) detect interactions with Ca²⁺ by a shift in the temperature of peak fluorescence in the presence of Ca²⁺ compared to EGTA. (F) The Ca²⁺ dissociation constants (K_m) of the recombinant ELC1 proteins shown in panel E ± standard deviations (SD).

described above (Fig. 6A). Expression of the mutant and wild-type versions of DDTy-ELC1 was evaluated after growing the parasites in the presence of ATc (as described earlier) and Shld-1 for 10 h followed by immunofluorescence microscopy. Staining of intracellular parasites with anti-Ty antibodies revealed expression and peripheral localization of DDTy-ELC1, R8A, and D15A, suggesting that none of the mutations studied affected localization or, therefore, their association with the glideosome (Fig. 6B).

As a first step to determine the effect of each mutation on parasite processes, we assessed the ability of intracellular vacuoles to egress when stimulated with Ca²⁺ ionophore A23187 for 2.5 min before fixing and examining were performed. While the expression of wild-type DDTy-ELC1 rescued the egress block observed for ATc-treated cDKO-ELC parasites, expression of mutants R8A and D15A restored egress only partially (Fig. 6C). Similarly, expression of the mutants in ATc-treated

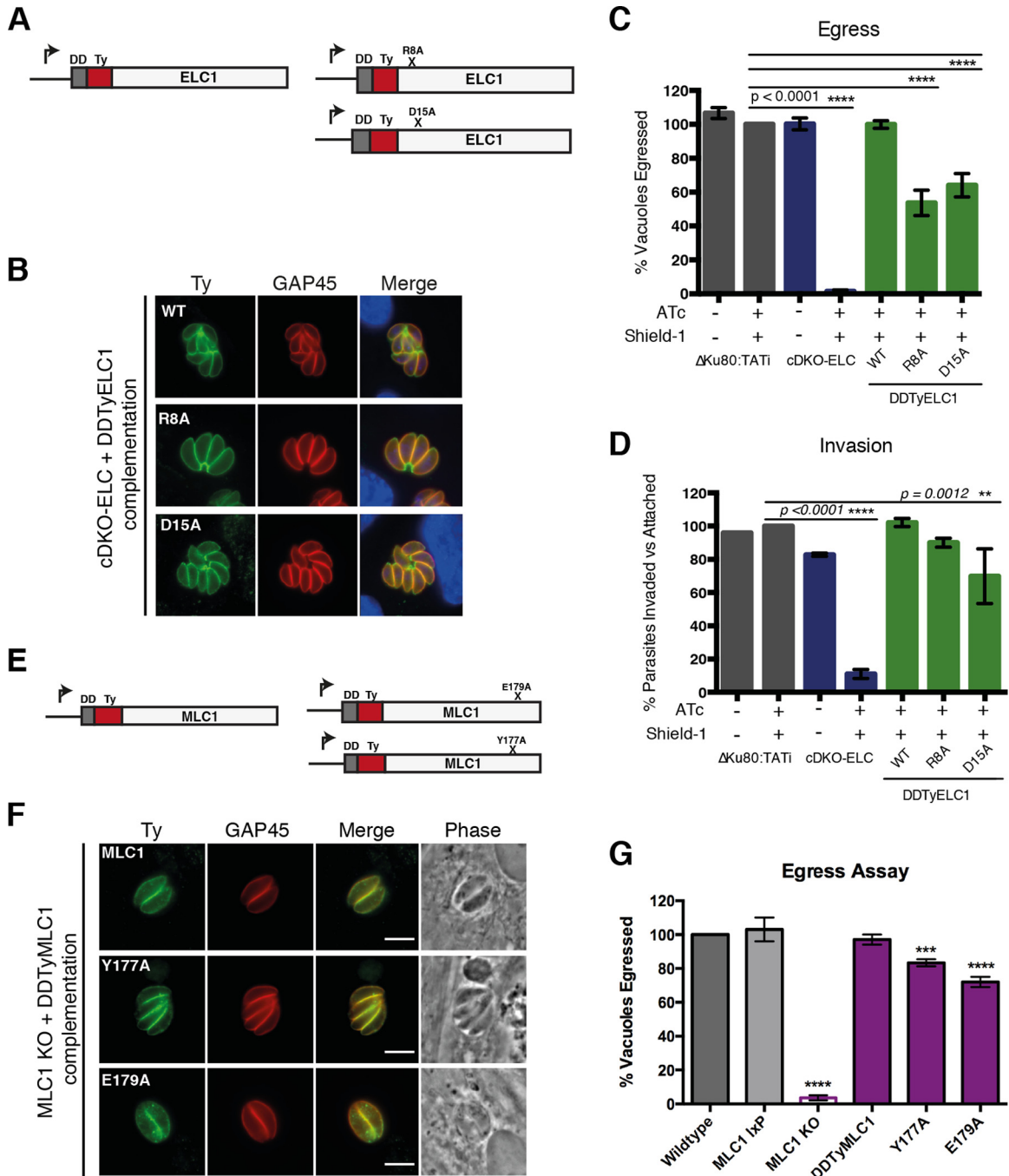


FIG 6 Molecular dissection of predicted interactions at the MyoA lever arm. (A) Schematic representation of ectopic versions of ELC1. N-terminal DDTy tags were fused to the ELC1 coding sequence, and mutations of key residues were introduced. (B) Immunofluorescence microscopy of intracellular cDKO-ELC parasites stably expressing ectopic wild-type and mutant DDTyELC1 proteins by the use of anti-Ty antibodies (green) and anti-GAP45 antibodies (red). (C and D) Parasites grown with or without 1.0 $\mu\text{g/ml}$ ATc for 96 h and with 1.0 μM Shld-1 for at least 8 h prior to experiments. (C) Fixed-egress assay performed on intracellular vacuoles grown for 30 h prior to stimulation with 8 μM A23187 for 2.5 min. At least 100 vacuoles were counted per slide. WT, wild type. (D) Two-color invasion assay performed to determine percentages of invaded parasites after a 30-min infection period. Numbers of invaded and total parasites were counted from >5 fields per slide. (E) Schematic representation of ectopic MLC1. N-terminal DDTy tags were fused to the MLC1 coding sequence, and mutations of key residues (Fig. 5A) were introduced. (F) Immunofluorescence microscopy of complemented MLC1 proteins with anti-Ty demonstrates peripheral localization and costaining with glideosome marker anti-GAP45. Bars, 5 μm . (G) Egress assay of MLC1 KO parasites (11) expressing wild-type and mutant MLC1 as shown in panel E. Parasites were treated with 50 μM rapamycin for 4 h and then grown without rapamycin for ~ 96 h prior to egress. DDTyMLC1 proteins were stabilized by 1.0 μM Shld-1 for >8 h prior to egress. The experiments represented in panels C, D, and G used duplicate (C and D) or triplicate (G) slides per experiment. Columns represent mean percentages of the results from 3 to 4 independent experiments. Error bars represent \pm SEM.

cDKO-ELC parasites could not fully restore invasion capability (Fig. 6D).

As we were unable to test the predicted interaction between ELC1 and MLC1 in the ADP-bound state by mutating ELC1, given that the interaction involves the ELC1 backbone, we instead investigated this interaction by mutating MLC1 residues. MLC1-E179 is predicted to form a hydrogen bond with the ELC1 and ELC2 backbones (Fig. 5A and C). An earlier iteration of the structural model also predicted an interaction of MLC1-Y177 with ELC1 EF1, and yet the refined model shows this residue pointing toward MLC1 itself. For the purpose of comparison, we mutated both these residues. To generate a complementation system for MLC1, we rederived the MLC1 DiCre KO line (loxpMLC1) recently reported (12) and excised the *mlc1* gene upon addition of rapamycin (Sigma-Aldrich). We then integrated the wild-type DDTyMLC1 or the Y177A and E179A mutants into the *uprt* locus of this strain (Fig. 6E). Expression and localization of the complementing copies of MLC1 were confirmed by immunofluorescence microscopy using anti-Ty antibodies. Peripheral staining of Ty was observed in all lines, and Ty colocalized with anti-GAP45 (Fig. 6F). Next, loxpMLC1 parasites and DDTyMLC1 mutant and wild-type complemented parasites were treated with 50 μ M rapamycin 96 h prior to egress to induce deletion of endogenous MLC1. Previously, deletion of MLC1 was reported to cause a complete block of egress (12). In agreement, we observed egress of only \sim 3.5% of rapamycin-treated loxpMLC1 vacuoles compared to untreated or wild-type controls (Fig. 6G). Expression of DDTyMLC1 fully restored egress capability and expression of DDTyMLC1 mutants partially restored this ability (Fig. 6G). The greatest defect in egress was observed when E179 was mutated, resulting in \sim 72% of the level of wild-type egress (Fig. 6G). As expected, the phenotypic defect in egress upon mutation of Y177 (\sim 83% egress) was not as significant as that seen with mutation of E179 but could have been due to disrupting its interactions with other hydrophobic residues, which may affect the rigidity of the MLC1 loop.

Given the major role that MyoA plays during *Toxoplasma* motility, we performed an in-depth analysis of parasite movement to more thoroughly understand the role of the ELC1-MLC1 interaction during pathogenicity. *Toxoplasma* spp. display three main types of motility (circular, twirling, and helical) on a two-dimensional (2D) surface, and live video microscopy was used to track and quantify these behaviors in the wild-type line (see Video S3 in the supplemental material) versus the mutant lines (Fig. 7). Parasites deficient in essential light chains showed only 20% of the gliding frequency of the parental control strain (Fig. 7A; see also Video S4). Motile cDKO-ELC parasites were uncoordinated (Video S5) or were limited to a short semicircle of motion (Video S6). Those that did move traveled a short distance only (Fig. 7C) and were remarkably slow (Fig. 7D). Parasites expressing ectopic DDTyELC1 showed reconstitution of the motility behaviors and parameters measured (Fig. 7; see also Video S7). Interestingly, however, ELC1 R8A and D15A mutants showed intermediary levels of total motile parasites (Fig. 7A), as well as a greater frequency of uncoordinated motility and twirling movement, but less helical movement, especially in the D15A mutant (Fig. 7B) (see Video S8 and Video S9, respectively). On average, those that moved glided shorter distances and at lower speeds such that the R8A mutant showed a greater spread of variability of these parameters than D15A (Fig. 7C and D).

Recent work has demonstrated that *Plasmodium* sporozoites

move in a stop-and-go fashion, with periods of rapid movement followed by periods of slow movement, which are best quantified by plotting the instantaneous speed versus time (30). We decided to see if *Toxoplasma* exhibited the same rhythmic pattern of motility and could be used as a measure of MyoA lever arm function. By plotting of the instantaneous velocity of gliding parasites, we saw that the parental line (Δ Ku80:TATi) displayed oscillating instantaneous speeds, where the velocity reached a maximum of \sim 5 μ m/s at a frequency of about 3 rounds per 20 s (Fig. 7E, panel i). Parasites depleted of both ELCs showed many fewer oscillations with a very low maximal velocity (Fig. 7E, panel ii). While complementation with wild-type ELC1 resulted in kinetic parameters similar to those seen with the parental lines (Fig. 7E, panel iii), ELC1 R8A showed a lower peak velocity with the same frequency of bursts of motility (Fig. 7, panel iv). ELC1 D15A showed the biggest changes in behavior, showing changes in maximal velocity as well as in the frequency of motility oscillations (Fig. 7E, panel v). Overall, our in-depth analysis shows that the coordination of Ca^{2+} binding by ELC1 and the interaction between the two light chains of the MyoA lever arm are critical to maintain robust and frequent motility of *Toxoplasma* across a 2D surface.

DISCUSSION

Gliding motility is critical to the virulence of apicomplexan parasites such as *Toxoplasma* and *Plasmodium* spp. (12, 28, 31). Motility involves the coordinated action of parasite transmembrane adhesins, actin, actin regulators, and the MyoA-based motor termed the glideosome, which generates the force required for motility (32). The experimental tractability of *Toxoplasma*, together with advances in genetic techniques, has led to extensive characterization of the glideosome and its components, and yet the mechanisms that regulate its activity and, thus, force production are still unknown. Motility is initiated in response to intracellular Ca^{2+} signaling events, and reports have shown glideosome components MyoA, MLC1, and GAP45 to be phosphorylated at several sites in a Ca^{2+} -dependent manner (19). As many conventional myosins, such as scallop and *Physarum* myosin II, are regulated by Ca^{2+} -dependent phosphorylation of the regulatory light chain or direct binding of Ca^{2+} to the essential light chain (14–18), it is possible that the *Toxoplasma* MyoA lever arm (MyoA neck-light chain complex) is similarly a regulatory site.

We have identified two essential light chains, previously ELC1 (19) and here ELC2, and show that both interact with the MyoA neck *in vitro* and *in vivo*. These essential light chains, together with MLC1 and the MyoA neck region, define the lever arm (Fig. 8), and the data have allowed us to investigate the role of this domain in *Toxoplasma* gliding motility. In the absence of a structure, we derived a model of the MyoA-ELC1/2-MLC1 complexes using homology modeling and molecular dynamic simulations and identified the region of the MyoA neck where ELC1 and ELC2 bind, and the findings were confirmed by *in vivo* experiments.

Using the tetracycline conditional-knockout system, we show that ELC1 and ELC2 have redundant roles in the MyoA glideosome but that their shared role is important for all glideosome-dependent processes. Our results also confirm that ELC1 and ELC2 interact with MyoA in a mutually exclusive manner and share the same binding site (Fig. 8), reflecting an emerging theme of redundancy and plasticity in the apicomplexan invasion and motility machinery. In agreement with these results, recent studies

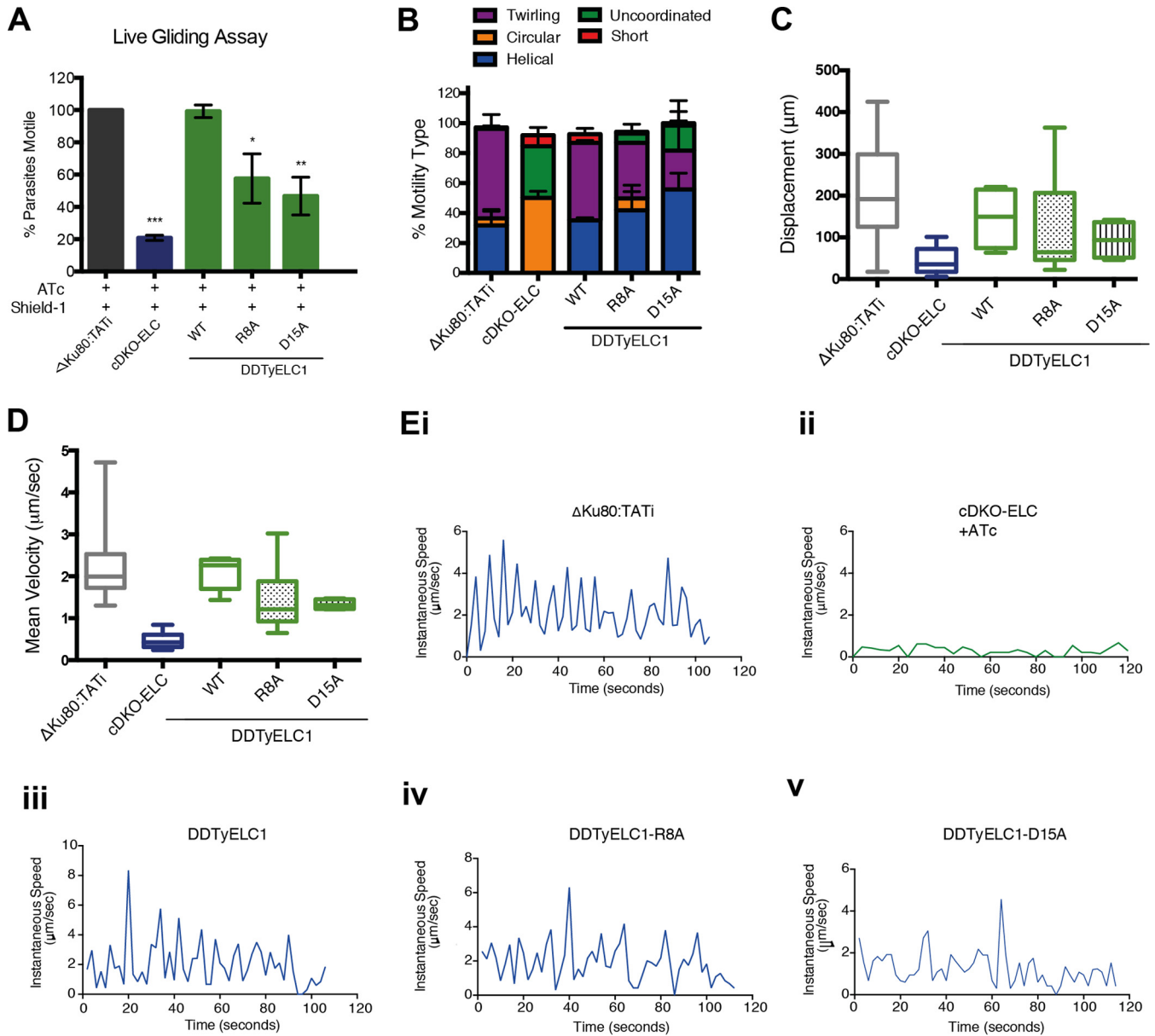


FIG 7 Intermolecular interactions at the MyoA lever arm are important for *Toxoplasma* gliding motility. Tachyzoite motility assays were performed by live video microscopy. (A and B) Mean percentages of motile parasites counted for 2 to 3 videos/experiment and for 3 separate experiments. Error bars represent \pm SEM. (C and D) Mean values were determined by automatic tracking of individual parasites using the MTrackJ plugin for ImageJ. Values were determined from 2 to 3 videos/experiment, where $n = 3$ independent experiments. Error bars represent \pm SEM. (E) Instantaneous speed of representative individual parasites tracked as described for panels C and D.

have demonstrated that at least one additional myosin contributes to *Toxoplasma* motility (12, 33). MyoC localizes to the basal complex of tachyzoites, where it also interacts with ELC1 and MLC1 as well as with GAP proteins and is able to partially compensate for the loss of MyoA by relocalizing along the parasite periphery (33). Furthermore, deletion of the MyoC gene in tachyzoites that lack MyoA results in greater defects in their ability to glide, invade, and egress, despite not leading to any impairment when MyoC was deleted alone (12, 33). As ELC1 is now confirmed to associate with both MyoA and MyoC (33), it is possible that simultaneous removal of ELC1 and ELC2 may in fact disrupt the function of both myosins, potentially explaining why the deletion of both essential

light chains leads to a more severe defect in some motility-dependent processes than deletion of MyoA alone (13). The possibility also remains that either of the two essential light chains could interact with other *Toxoplasma* myosins and/or other IQ motif-containing proteins, as has been shown previously for human and fly ELCs (34, 35). In the latter case, the conditional removal of endogenous or introduction of mutant essential light chain presented in this study may also affect unknown cellular processes. The concept of redundancy and plasticity was also recently established in the invasion pathway for the AMA-RON pairs (36), and, given the redundancy and plasticity of the ELCs shown here, together with that discovered for the glideosome

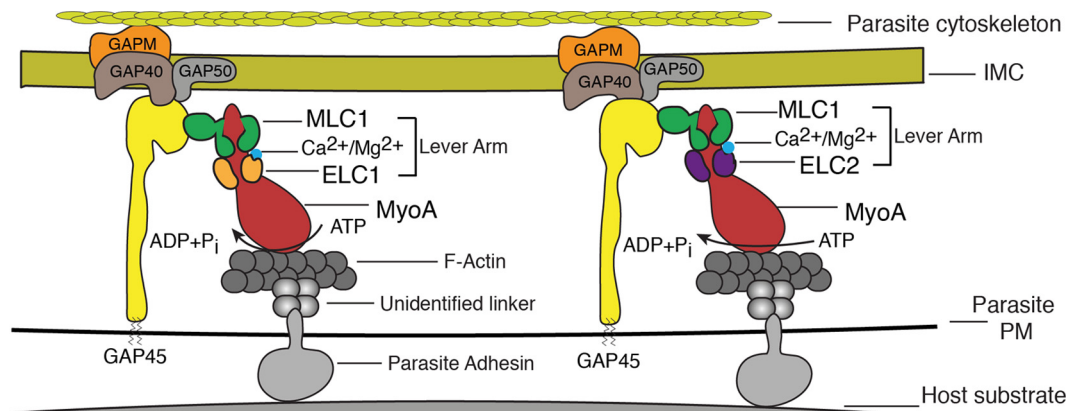


FIG 8 Model of the *Toxoplasma* MyoA glideosome. The composition of the MyoA glideosome in *Toxoplasma* tachyzoites, localized at the parasite periphery in the space between the plasma membrane (PM) and inner membrane complex (IMC), is shown.

components MyoA/C (12, 33) and GAP45/GAP70/GAP80 (3, 33), it is likely that a greater level of complexity exists to ensure the production of force for motility in a complex physiological setting. One important difference exists, however, between what we have found with ELC1 and ELC2 and the redundant mechanisms in other components as outlined above. Both ELC1 and ELC2 appear to be associated (in a mutually exclusive manner) with the glideosome under physiological conditions, while other redundant mechanisms have been observed only upon the genetic removal of other components.

Myosin lever arms can be regulated by direct or indirect Ca^{2+} -dependent mechanisms. The direct interaction of ELCs with Ca^{2+} is one such method, and the presence of putative EF hands on both ELC1 and ELC2 provided the first insight that the essential light chains may regulate glideosome activity by interacting directly with Ca^{2+} . We compared structural models containing the two essential light chains and found that, as expected, the Ca^{2+} -binding regions were conserved. Therefore, we performed a detailed investigation of only a single essential light chain, ELC1. We confirmed that ELC1 has the ability to directly bind Ca^{2+} *in vitro* at EFI by using *E. coli*-expressed wild-type ELC1 in comparison with an EFI mutant. Furthermore, we then investigated the importance of the residues involved in this interaction *in vivo* by assessing the effect of residue mutation on gliding motility, invasion, and egress. In agreement with our model, disruption of a key residue predicted to coordinate Ca^{2+} activity impaired all gliding-dependent processes tested. Despite these results, a recent convincing report by Bookwalter et al. showed that the presence of Ca^{2+} had no effect on the speed of *in vitro* motility of recombinant MyoA-ELC1-MLC1 complexes expressed and purified from insect cells (25). A possible explanation for these conflicting results is provided by the dissociation constant of ELC1 for Ca^{2+} determined in Fig. 5F. A Ca^{2+} dissociation constant of $\sim 38 \mu\text{M}$ is low, and if ELC1 can also interact with other divalent cations, EFI could instead be occupied by Mg^{2+} (Fig 8), which would be present at a higher concentration than free Ca^{2+} ions in the cellular environment. The results of replacement of Ca^{2+} with Mg^{2+} in the structural model presented here suggest that Mg^{2+} would behave similarly to Ca^{2+} . Such an interaction has been proven for MlcD, the light chain of *Dictyostelium discoideum* MyoD, which has dissociation constants of $52 \mu\text{M}$ for Ca^{2+} and $450 \mu\text{M}$ for Mg^{2+} . In cells,

MlcD interacts with Mg^{2+} and myosin motile activity is regulated by the concentration of free Mg^{2+} ions (37, 38).

The myosin lever arm is a critical point of rigidity, as the head domain pivots upon ATP hydrolysis to undertake the power stroke for force production and subsequent actin displacement (24, 39–41). In this paper, we present the first *in vivo* functional characterization of the ELCs that complete the MyoA lever arm complex and show their importance for MyoA stability and function. Our structural modeling suggests a possible mechanism for lever arm stabilization whereby Ca^{2+} binding to ELC1 or ELC2 could facilitate interactions between the two light chains ELC1/ELC2 and MLC1, thus rigidifying the lever arm region (Fig. 8). A similar ELC-regulatory light chain (RLC) interface has been shown by Ni et al. to be important for nonmuscle myosin II activity and proposed to be facilitated by phosphorylation of the RLC (42). We performed a set of functional readouts to test these specific hypotheses related to key interactions between the different lever arm components. Our mutational results confirmed that the key residues predicted to coordinate these interactions contributed to MyoA fidelity *in vivo*, supporting the idea of a role for the MyoA lever arm in gliding motility. Likewise, *in vitro* experiments by Bookwalter et al. showed that addition of recombinant ELC1 to a MyoA-MLC1 complex doubled actin filament displacement velocity *in vitro* (25), while earlier work demonstrated that deletion of the last 55 C-terminal residues of MyoA completely prevented movement of actin filaments with no detrimental effect on ATPase activity or actin binding capacity shown by the MyoA head (7).

Our report identifies ELC2 and shows the importance of an essential light chain to *Toxoplasma* gliding motility. Furthermore, it presents an *in vivo*-validated model of the MyoA lever arm complex, highlighting key residues for lever arm function that are conserved in ELC1 and ELC2 and offering a mechanistic model for how the lever arm is stabilized to perform the power stroke to generate productive motility.

MATERIALS AND METHODS

Cloning of DNA constructs. Refer to Table S1 in the supplemental material for all primer information.

Construction of ELC conditional KOs. The ELC1 and ELC2 conditional KO constructs pPR2-3HA-ELC1 and pPR2-3HA-ELC2 were cre-

ated by amplifying the 5' flanks of the *elc1* and *elc2* open reading frame (ORF) from *T. gondii* RH strain genomic DNA (gDNA), using primer pairs 1/2 and 3/4, respectively. The 5' flanks were inserted into the pPR2-3HA vector with restriction enzymes NdeI and NsiI, and integration was confirmed by PCR with primer pairs 5/7 and 6/7. Similarly, the *elc1* and *elc2* 3' flanks were amplified from gDNA with primer pairs 8/9 and 10/11, respectively. The 3' flanks were inserted into the vector using XmaI and NotI restriction sites, and integration was confirmed by PCR with primer pairs 12/14 and 13/14, respectively. To generate the ELC1 KO construct pCTY-ELC1 KO+LoxP, *elc1* 5' and 3' flanks were amplified from gDNA using primer pairs 15/16 and 19/20, respectively, and inserted into the pTCY-CAT-LoxP vector at restriction sites SpeI and AvrII. Integration of flanks was confirmed by PCR with primer pairs 17/18 and 21/22, respectively.

Generation of ELC complementing constructs. To generate the ELC complementation plasmid, an *uprt* 5' flank was first inserted into the pCTDDnTy vector (sequence available on request) by digestion with KpnI. Integration and orientation of the flank were determined by PCR with primers 23/18 and primers 24/18. The tubulin promoter was then replaced with the ELC1 promoter by amplifying the *elc1* 5' flank from gDNA with primer pair 25/26 and inserting it using SpeI and NdeI. Integration was confirmed with primers 27/178. The ELC1 and ELC2 coding sequences were amplified from cDNA with primer pairs 28/29 and 30/31, respectively, and inserted at restriction sites XmaI and PstI to create plasmids pCUEDDTy-ELC1 and pCUEDDTy-ELC2. To create ELC1 R8A and D15A mutants, mutagenesis PCR was performed with PfuTurbo C_x Hotstart DNA polymerase (Agilent Technologies) and pCUEDDTy-ELC1 with primer pairs 32/33 and 34/35, respectively.

Generation of MLC1 complementation constructs. The MLC1 complementation plasmids were created as described above. Briefly, the MLC1 coding sequence was amplified from cDNA using primer pair 39/40 and inserted into pCUEDDTy. MLC1 mutants Y177A and E179A were created as described above using primer pairs 41/42 and 43/44, respectively. pCUEDDTy-MLC1-E179A was used as the template for mutagenesis PCR, as described above, with primers 45/46. All plasmids were confirmed by sequencing and transformed in *E. coli* BetaDH10 cells.

MyoA neck-ELC interaction constructs. The *Toxoplasma* MyoA neck region (residues 771 to 831) and the truncated MyoA neck missing the ELC binding site were amplified from cDNA using primer pairs 36/37 and 38/37, respectively. They were inserted into the pCUEDDTy vector by digestion with XmaI and PstI to create pCUEDDTy-MyoA neck and pCUEDDTy-MyoA neck_{800–831}.

***E. coli* expression constructs.** The *Toxoplasma* MyoA neck region was amplified from pCUEDDTy-MyoA neck and cloned into the pHUE vector (55) to give an N-terminal His₆-ubiquitin fusion construct (H₆Ub-MyoA-neck). The gene encoding *Toxoplasma* ELC1 was amplified from pCUEDDTy-ELC1 and cloned into the pProEX HTb expression vector to give the pPro-ELC1 expression plasmid. The mutant forms of ELC1 (R8A and D15A) were amplified from plasmids pCUEDDTy-ELC1-R8A and -D15A and cloned into pProEX HTb. All plasmids were confirmed by sequencing and transformed into *E. coli* BL21(DE3) cells.

Tagging of endogenous MyoA with HSF. A construct containing His-StrepII-Flag (HSF)-tagged MyoA was created using the vector pLIC-CAT-3HA-LoxP. The MyoA promoter was amplified with primers 50/51 and digested with AflII and AatII. The StrepII-Flag sequence was amplified from pLIC-SF-TAP using primers 52/53 and a tobacco etch virus (TEV) sequence inserted 3' with the antisense primer and then digested with AatII and EcoRV. The MyoA coding sequence was amplified from cDNA with primers 54/55 and digested with EcoRV and NsiI. The three products were then inserted into the vector as described above to create pLIC-CAT-MyoA5'-HSFMyoA-LoxP. An alternative version was created by replacing the chloramphenicol acetyltransferase (CAT) cassette with the phleomycin resistance gene BLE to create pLIC-BLE-MyoA5'-HSFMyoA-LoxP.

Transfection. Tachyzoites were transfected using standard procedures. Freshly lysed parasites were collected at $\sim 10^7$ cells/transfection and suspended in 400 μ l CytoMix (120 mM KCl, 0.15 mM CaCl₂, 2 mM EGTA, 5 mM MgCl₂, 10 mM K₂HPO₄ and KH₂PO₄, 25 mM HEPES, pH 7.6) to which 50 μ g circular or 20 μ g linear plasmid DNA was added. The mix was electroporated at 25 μ F and 1.5 kV with a Gene Pulser II system (BioRad) using a 2-mm-gap electrode cuvette (Cell Projects).

Cell culture. Human foreskin fibroblasts (HFFs) (ATCC) were maintained in Dulbecco's modified Eagle's medium (DMEM) supplemented with 10% (vol/vol) cosmic calf serum (HyClone) at 37°C and 10% CO₂. *Toxoplasma* tachyzoites were maintained by growth in HFF monolayers using DMEM supplemented with 1% (vol/vol) fetal bovine serum and 1% (vol/vol) GlutaMAX (Gibco) at 37°C and 10% CO₂.

IFAs. Immunofluorescence assays (IFAs) were performed using standard procedures. Briefly, intracellular parasites were fixed in 4% paraformaldehyde, permeabilized in 0.1% Triton X-100-phosphate-buffered saline (PBS), and blocked in 3% bovine serum albumin (BSA)-PBS. Specified primary antibodies were diluted in 3% BSA-PBS, decorated onto blocked slides, and detected with antibodies conjugated to Alexa Fluor 594 or 488 (Molecular Probes). Parasites were then imaged on a Zeiss inverted wide-field microscope equipped with AxioCam MRM and AxioVision (release 4.8) with Deconvolution software.

Coimmunoprecipitation and Western blot analysis. Parasites were collected promptly after lysis from HFF monolayers and pelleted by centrifugation. All procedures were then performed on ice or at 4°C. Protein was extracted in IP buffer (20 mM HEPES, 0.15 M NaCl, 1% [vol/vol] Triton X-100, and 0.5% NP-40 [pH 7.4] with 1 complete protease inhibitor cocktail [Roche]), and insoluble material was separated by centrifugation at 55,000 rpm. A 1:100 dilution of the required antibody was added to 50- μ l protein G Sepharose and incubated with agitation for 30 min. Lysate was added to the Sepharose-antibody mix and agitated at 4°C for 1 to 2 h. Immunoprecipitation was performed by centrifugation, and the reaction mixture was eluted in 2 \times reducing sample buffer. Eluates were resolved by SDS-PAGE with 4% to 12% NuPage bis-Tris gels (Invitrogen) and run at 150 V (Invitrogen Surelock electrophoresis cell) in MOPS (morpholinepropanesulfonic acid) running buffer (Invitrogen). Proteins were transferred from the bis-Tris gels to a nitrocellulose membrane and then blocked in blocking solution (5% [wt/vol] skim milk powder [Denville]-PBS) for 1 h at room temperature. The desired primary antibody was diluted in blocking solution and used to probe membranes for 1 h at room temperature or 4°C overnight. Membranes were incubated in goat anti-rabbit or anti-mouse horseradish peroxidase (HRP) (Millipore or Southern Biotech, respectively) diluted in blocking solution for 1 h at room temperature. Membranes were washed 4 times for 10 min each time in 0.05% human tonicity PBS-Tris (HTPBST) and then immersed in Amersham ECL Western blotting detection reagents (GE Healthcare) for 1 min. Proteins were detected by exposing membranes to Super RX medical X-ray film (Fuji Film) using a Kodak X-Omat 3000RA processor.

Homology modeling and molecular dynamics. Homology models were built using the Modeller program (version 9.12) (43) and structures of scallop myosin as the templates (PDB codes 1KK8 and 3E3R for the ADP-bound model and PDB code 1B7T for the ATP-bound model).

Molecular dynamics (MD) simulations were carried out using the GROMACS package (version 4.5.7) (44) and the optimized potential for liquid simulation/all atom (OPLS/AA) force field (45). Ionizable residues were assumed to be in their standard state at neutral pH. The complex was placed in a 115-by-115-by-210-Å (45) TIP4P (46) water box, and water molecules were replaced by K⁺ and Cl⁻ ions to neutralize the system and produce an ionic concentration of 0.1 M. Protein and solvent were coupled separately to a thermal bath at 300 K using a Berendsen thermostat (47) applied with a coupling time of 0.1 ps; a Berendsen barostat (47) at 1 bar with a coupling time of 0.5 ps was also included. All of the simulations were performed with a single nonbonded cutoff of 10 Å, applying a neighbor list update frequency of 10 steps (20 fs). The particle mesh Ewald method (48) was used to account for long-range electrostatics, applying a

grid width of 1.2 Å and a fourth-order spline interpolation. Bond lengths were constrained using the LINCS algorithm (49).

All simulations consisted of an initial minimization of water molecules followed by 200 ps of MD simulations with the protein fixed. After removing all the restraints on the protein, MD simulations were continued for 20 ns. The last 20-ns simulation was analyzed using standard GROMACS tools.

Ca²⁺-binding free energies were estimated using the GROMACS umbrella sampling protocol. Starting structures were generated by the use of a pulling simulation using a force constant of 1,000 kJ/(mol nm²) at a rate of 1 nm/ns; the Ca²⁺ ion was pulled away from its binding pocket (defined by the alpha-carbons of the amino acids of the binding loop), and rotation of the system was prevented using the enforced-rotation function with a force constant of 500 kJ/(mol nm²). A total of 26 structures were selected as umbrella sampling windows. They were equilibrated as described above. A 5-ns simulation was performed in each window for a total simulation time of 130 ns for umbrella sampling. Analysis of results was performed with the weighted-histogram analysis method (WHAM) (50).

In vitro protein expression and purification. *E. coli* BL21(DE3) cells were grown in Terrific broth containing 100 µg/ml carbenicillin at 37°C to an optical density at 600 nm (OD₆₀₀) of ~0.6, moved at 18°C for 30 min, and induced with 0.2 mM IP for 16 h. The cells were harvested by centrifugation (7,000 × g, 10 min) and stored at -80°C until needed. To purify ELC1 and the R8A and D15A mutants, cell pellets were resuspended in buffer A (50 mM Tris-HCl [pH 7.5], 300 mM NaCl, 10 mM imidazole, 5 mM 2-mercaptoethanol, and 1 mM phenylmethylsulfonyl fluoride [PMSF]) and lysed by sonication. Cell debris was removed by centrifugation at 25,000 × g for 30 min and the supernatant applied to a 1-ml bed volume of nickel-nitrilotriacetic acid (Ni-NTA) agarose resin (Qiagen) preequilibrated in buffer A. After washing with 5 column volumes of buffer A was performed, the sample was eluted with buffer supplemented with 100 mM imidazole. The protein was then loaded onto a size exclusion Superdex 200 10/300-GI column (GE Healthcare) preequilibrated in buffer B (50 mM Tris-HCl [pH 7.5] and 250 mM NaCl), and the peak fractions were pooled, concentrated, and stored at -80°C after the addition of 20% glycerol.

The purification of the H₆Ub-MyoA-tail construct was done as follows. The frozen cell pellet was resuspended in buffer C (50 mM Tris-HCl [pH 7.5], 300 mM NaCl, 10 mM imidazole, 10 mM 2-mercaptoethanol, 30% glycerol, and 1 mM PMSF) and lysed by sonication. Unbroken cells and debris were removed by centrifugation at 25,000 × g for 30 min, and the supernatant was applied to a 1-ml bed volume of Ni-NTA agarose resin (Qiagen) preequilibrated in buffer C. After washing of the resin with 5 column volumes of buffer C supplemented with 20 mM imidazole was performed, the protein was eluted in buffer D (50 mM Tris-HCl [pH 7.5], 150 mM NaCl, 200 mM imidazole, 1 mM 2-mercaptoethanol, and 30% glycerol). Finally, the protein was loaded onto a size exclusion Superdex 200 column preequilibrated in buffer E (10 mM HEPES [pH 7.4], 150 mM NaCl, 50 µM EDTA, and 15% glycerol) and the fractions with the H₆Ub-MyoA-tail protein were pooled, snap frozen in liquid nitrogen, and stored at -80°C until needed.

Thermal shift assay. Binding of Ca²⁺ to ELC1 and its R8A and D15A mutants was assayed using thermal-shift assays and a Rotor-Gene 3000 real-time PCR machine. The proteins were diluted to a 20 µM final concentration in buffer F (50 mM Tris-HCl [pH 7.5] and 50 mM NaCl) containing increasing amounts (10⁻⁸ to 10⁻³ M) of CaCl₂ in a total reaction volume of 25 µl. The fluorescent probe Sypro Orange (Sigma) was diluted 1:100 in dimethyl sulfoxide (DMSO), and 1 µl was added per sample just before the run. The temperature was raised in 1°C/min steps from 28°C to 85°C, and fluorescence readings were recorded (excitation, 465 nm; emission, 580 nm). For data analysis, fluorescence was plotted against temperature, and the melting temperature (T_m) of the sample was calculated by fitting the sigmoidal melt curve to the Boltzmann equation as implemented in GraphPad Prism. Data points after the maximum fluorescence intensity were excluded from the fitting. The change in T_m as a

function of the logarithm of the Ca²⁺ concentration resulted in a sigmoidal plot, where the half-maximal effective concentration (EC₅₀) was taken to be equal to the Ca²⁺ affinity (K_d [dissociation constant]). Two or more independent titrations were performed for each protein sample.

Egress assay. Parasites were pretreated for 66 h ± 1.0 µg/ml ATc and then inoculated onto new s and continued to grow for 30 h with or without ATc and/or 1.0 µM shield-1. Egress was stimulated by incubating parasite-infected HFFs with DMEM containing 0.06% DMSO or 8 µM Ca²⁺ ionophore A23187 from *Streptomyces chartreusensis* (Calbiochem) for 2.5 min at room temperature before fixation with paraformaldehyde (PFA) was performed. IFA was performed as described above with mouse anti-SAG1 antibodies. The average number of ruptured vacuoles was determined by counting a minimum of 100 vacuoles per each slide using duplicate or triplicate slides for each experiment. Three independent experiments were performed.

Two-color invasion assay. Parasites were grown in HFF cells for 96 h in the presence and absence of 1.0 µg/ml ATc and 1.0 µM Shld-1. Freshly lysed parasites were collected and filtered through a 27-gauge needle to release the remaining intracellular parasites. Parasites were counted and adjusted to 2.5 × 10⁷ cells/ml in warm DME medium with 10 mM HEPES (pH 7.4). The parasite cell suspension was inoculated onto a new confluent monolayer of HFF cells and grown on glass slides in 24-well plates at 200 µl/well in duplicate or triplicate wells. The plate was spun at 1,000 rpm for 1 min to deposit parasites onto the HFF monolayer. Invasion was allowed to proceed for 30 min by incubation at 37°C and 10% CO₂. After incubation, cells were fixed for 10 min in 2.5% PFA-0.06% glutaraldehyde-HPBS. A two-color immunofluorescence assay was then performed as described previously (51). Extracellular parasites were probed with anti-SAG1, and all parasites were stained using anti-GAP45 antibodies. Total numbers of parasites and extracellular parasites were counted for 5 fields of view per slide. Duplicate or triplicate slides were counted for each experiment. Three independent experiments were performed.

Live gliding-motility assay. Freshly egressed parasites were harvested and resuspended in warm Endo buffer (44.7 mM K₂SO₄, 10 mM MgSO₄, 106 mM sucrose, 5 mM glucose, 20 mM Tris-H₂SO₄, 3.5 mg/ml BSA, pH 8.2) and settled onto glass-bottom culture chamber slides (ibidi) coated with 10 µg/ml poly-L lysine-PBS. After the parasites had settled, Endo buffer was slowly aspirated from the chamber and replaced with warm gliding buffer (1 mM EGTA, 20 mM HEPES [pH 7.5], DMEM). Images were collected in 2-s intervals for a minimum of 2 min. Time-lapse video microscopy was conducted using a Zeiss Live Scan microscope equipped with a temperature-controlled chamber to maintain 37°C incubation. Images were collected using phase contrast under conditions of low-light illumination and an AxioCam MR camera at ×40 magnification, using AxioVision release 4.8 software to control the shutters and camera. Manual tracking of parasites was achieved with the MTrackJ plugin for ImageJ. Videos were generated using ImageJ software. Motility analyses were performed as reported previously (52–54).

Statistical analyses. Graphs were prepared and statistical analyses performed using Prism 6 software. All results are presented as mean values ± standard errors of the means (SEM) of the results of at least 3 independent experiments. Parametric comparisons were tested for statistical significance using unpaired, equal variance, two-tailed Student's *t* tests. The Mann-Whitney test was used for nonparametric comparisons.

Accession numbers. The EuPathDB gene accession number for the ELC2 sequence presented in this paper is TGME49_305050 (previously TGME49_105050). That for the ELC1 sequence is TGME49_269442 (previously TGME49_069440).

SUPPLEMENTAL MATERIAL

Supplemental material for this article may be found at <http://mbio.asm.org/lookup/suppl/doi:10.1128/mBio.00845-15/-DCSupplemental>.

Video S1, MPG file, 10.3 MB.

Video S2, MPG file, 9.4 MB.

Video S3, AVI file, 8.8 MB.

Video S4, AVI file, 5.9 MB.
 Video S5, AVI file, 0.2 MB.
 Video S6, AVI file, 0.4 MB.
 Video S7, AVI file, 3.3 MB.
 Video S8, AVI file, 5.8 MB.
 Video S9, AVI file, 8.9 MB.
 Table S1, DOCX file, 0.1 MB.

ACKNOWLEDGMENTS

We thank the following people for antibodies used in this study: D. Soldati-Favre (anti-MLC1 and anti-MyoA), C. Beckers (anti-GAP45), and K. Gull (BB2 mouse anti-Ty monoclonal). We also thank G. van Dooren for sharing unpublished plasmids.

M.J.W. is a recipient of an Australian Postgraduate Award, and C.J.T. is an ARC/NHMRC Future Fellow. This work was supported by a National Health and Medical Research Council project grant (GNT1025598). B.S. is supported by NIH RO1 AI 64671 and AI084415. B.S. is a GRA distinguished investigator. This work was also made possible through Victorian State government Operational Infrastructure Support and the Australian government (NHMRC IRIISS).

REFERENCES

- Torgerson PR, Mastroiacovo P. 2013. The global burden of congenital toxoplasmosis: a systematic review. *Bull World Health Organ* 91:501–508. <http://dx.doi.org/10.2471/BLT.12.111732>.
- Gaskins E, Gilk S, DeVore N, Mann T, Ward G, Beckers C. 2004. Identification of the membrane receptor of a class XIV myosin in *Toxoplasma gondii*. *J Cell Biol* 165:383–393. <http://dx.doi.org/10.1083/jcb.200311137>.
- Frénil K, Polonais V, Marq J-B, Stratmann R, Limenitakis J, Soldati-Favre D. 2010. Functional dissection of the apicomplexan glideosome molecular architecture. *Cell Host Microbe* 8:343–357. <http://dx.doi.org/10.1016/j.chom.2010.09.002>.
- Baum J, Richard D, Healer J, Rug M, Krnajska Z, Gilberger T-W, Green JL, Holder AA, Cowman AF. 2006. A conserved molecular motor drives cell invasion and gliding motility across malaria life cycle stages and other apicomplexan parasites. *J Biol Chem* 281:5197–5208. <http://dx.doi.org/10.1074/jbc.M509807200>.
- Bullen HE, Tonkin CJ, O'Donnell RA, Tham W-H, Papenfuss AT, Gould S, Cowman AF, Crabb BS, Gilson PR. 2009. A novel family of apicomplexan glideosome-associated proteins with an inner membrane-anchoring role. *J Biol Chem* 284:25353–25363. <http://dx.doi.org/10.1074/jbc.M109.036772>.
- Johnson TM, Rajfur Z, Jacobson K, Beckers CJ. 2007. Immobilization of the type XIV myosin complex in *Toxoplasma gondii*. *Mol Biol Cell* 18:3039–3046. <http://dx.doi.org/10.1091/mbc.E07-01-0040>.
- Herm-Götz A, Weiss S, Stratmann R, Fujita-Becker S, Ruff C, Meyhöfer E, Soldati T, Manstein DJ, Gees MA, Soldati D. 2002. *Toxoplasma gondii* myosin A and its light chain: a fast, single-headed, plus-end-directed motor. *EMBO J* 21:2149–2158. <http://dx.doi.org/10.1093/emboj/21.9.2149>.
- Bergman LW, Kaiser K, Fujioka H, Coppens I, Daly TM, Fox S, Matuschewski K, Nussenzweig V, Kappe SH. 2003. Myosin A tail domain interacting protein (MTIP) localizes to the inner membrane complex of *Plasmodium* sporozoites. *J Cell Sci* 116:39–49. <http://dx.doi.org/10.1242/jcs.00194>.
- Jewett TJ, Sibley LD. 2003. Aldolase forms a bridge between cell surface adhesins and the actin cytoskeleton in apicomplexan parasites. *Mol Cell* 11:885–894. [http://dx.doi.org/10.1016/S1097-2765\(03\)00113-8](http://dx.doi.org/10.1016/S1097-2765(03)00113-8).
- Starnes GL, Coincon M, Sygusch J, Sibley LD. 2009. Aldolase is essential for energy production and bridging adhesion-actin cytoskeletal interactions during parasite invasion of host cells. *Cell Host Microbe* 5:353–364. <http://dx.doi.org/10.1016/j.chom.2009.03.005>.
- Shen B, Sibley LD. 2014. *Toxoplasma* aldolase is required for metabolism but dispensable for host-cell invasion. *Proc Natl Acad Sci U S A* 111:3567–3572. <http://dx.doi.org/10.1073/pnas.1315156111>.
- Egarter S, Andenmatten N, Jackson AJ, Whitelaw JA, Pall G, Black JA, Ferguson DJ, Tardieux I, Mogilner A, Meissner M. 2014. The *Toxoplasma* acto-MyoA motor complex is important but not essential for gliding motility and host cell invasion. *PLoS One* 9:e91819. <http://dx.doi.org/10.1371/journal.pone.0091819>.
- Andenmatten N, Egarter S, Jackson AJ, Jullien N, Herman J-P, Meissner M. 2013. Conditional genome engineering in *Toxoplasma gondii* uncovers alternative invasion mechanisms. *Nat Methods* 10:125–127. <http://dx.doi.org/10.1038/nmeth.2301>.
- Zhang Y, Kawamichi H, Tanaka H, Yoshiyama S, Kohama K, Nakamura A. 2012. Calcium-dependent regulation of the motor activity of recombinant full-length *Physarum* myosin. *J Biochem* 152:185–190. <http://dx.doi.org/10.1093/jb/mvs062>.
- Zhang Y, Nakamura A, Kawamichi H, Yoshiyama S, Katayama T, Kohama K. 2010. Calcium regulation of the ATPase activity of *Physarum* and scallop myosins using hybrid smooth muscle myosin: the role of the essential light chain. *FEBS Lett* 584:3486–3491. <http://dx.doi.org/10.1016/j.febslet.2010.07.011>.
- Prochniewicz E, Pierre A, McCullough BR, Chin HF, Cao W, Saunders LP, Thomas DD, Prochniewicz E, Pierre A, McCullough BR, Chin HF, Cao W, Saunders LP, Thomas DD, De La Cruz EM. 2011. Actin filament dynamics in the actomyosin VI complex is regulated allosterically by calcium-calmodulin light chain. *J Mol Biol* 413:584–592. <http://dx.doi.org/10.1016/j.jmb.2011.08.058>.
- Himmel DM, Mui S, O'Neill-Hennessey E, Szent-Györgyi AG, Cohen C. 2009. The on-off switch in regulated myosins: different triggers but related mechanisms. *J Mol Biol* 394:496–505. <http://dx.doi.org/10.1016/j.jmb.2009.09.035>.
- Szent-Györgyi AG. 1996. Regulation of contraction by calcium binding myosins. *Biophys Chem* 59:357–363. [http://dx.doi.org/10.1016/0301-4622\(95\)00128-X](http://dx.doi.org/10.1016/0301-4622(95)00128-X).
- Nebi T, Prieto JH, Kapp E, Smith BJ, Williams MJ, Yates JR, Cowman AF, Tonkin CJ. 2011. Quantitative *in vivo* analyses reveal calcium-dependent phosphorylation sites and identifies a novel component of the *Toxoplasma* invasion motor complex. *PLoS Pathog* 7:e1002222. <http://dx.doi.org/10.1371/journal.ppat.1002222>.
- Green JL, Rees-Channer RR, Howell SA, Martin SR, Knuepfer E, Taylor HM, Grainger M, Holder AA. 2008. The motor complex of *Plasmodium falciparum*: phosphorylation by a calcium-dependent protein kinase. *J Biol Chem* 283:30980–30989. <http://dx.doi.org/10.1074/jbc.M803129200>.
- Kato N, Sakata T, Breton G, Le Roch KG, Nagle A, Andersen C, Bursulaya B, Henson K, Johnson J, Kumar KA, Marr F, Mason D, McNamara C, Plouffe D, Ramachandran V, Spooner M, Tuntland T, Zhou Y, Peters EC, Chatterjee A, Schultz PG, Ward GE, Gray N, Harper J, Winzler EA. 2008. Gene expression signatures and small-molecule compounds link a protein kinase to *Plasmodium falciparum* motility. *Nat Chem Biol* 4:347–356. <http://dx.doi.org/10.1038/nchembio.87>.
- Jacot D, Frénil K, Marq J-B, Sharma P, Soldati-Favre D. 2014. Assessment of phosphorylation in *Toxoplasma* glideosome assembly and function. *Cell Microbiol* 16:1518–1532. <http://dx.doi.org/10.1111/cmi.12307>.
- Tang Q, Andenmatten N, Hortua Triana MA, Deng B, Meissner M, Moreno SN, Ballif BA, Ward GE. 2014. Calcium-dependent phosphorylation alters class XIVa myosin function in the protozoan parasite *Toxoplasma gondii*. *Mol Biol Cell* 25:2579–2591. <http://dx.doi.org/10.1091/mbc.E13-11-0648>.
- Llinas P, Pylypenko O, Isabet T, Mukherjee M, Sweeney HL, Houdusse AM. 2012. How myosin motors power cellular functions—an exciting journey from structure to function: based on a lecture delivered at the 34th FEBS Congress in Prague, Czech Republic, July 2009. *FEBS J* 279:551–562. <http://dx.doi.org/10.1111/j.1742-4658.2011.08449.x>.
- Bookwalter CS, Kelsen A, Leung JM, Ward GE, Trybus KM. 2014. A *Toxoplasma gondii* class XIV myosin, expressed in Sf9 cells with a parasite co-chaperone, requires two light chains for fast motility. *J Biol Chem* 289:30832–30841. <http://dx.doi.org/10.1074/jbc.M114.572453>.
- Herm-Götz A, Agop-Nersesian C, Münter S, Grimley JS, Wandless TJ, Frischknecht F, Meissner M. 2007. Rapid control of protein level in the apicomplexan *Toxoplasma gondii*. *Nat Methods* 4:1003–1005. <http://dx.doi.org/10.1038/nmeth1134>.
- Brookman JL, Stott AJ, Cheeseman PJ, Burns NR, Adams SE, Kingsman AJ, Gull K. 1995. An immunological analysis of Ty1 virus-like particle structure. *Virology* 207:59–67. <http://dx.doi.org/10.1006/viro.1995.1051>.
- Meissner M, Schlüter D, Soldati D. 2002. Role of *Toxoplasma gondii* myosin A in powering parasite gliding and host cell invasion. *Science* 298:837–840. <http://dx.doi.org/10.1126/science.1074553>.
- Sheiner L, Demerly JL, Poulsen N, Beatty WL, Lucas O, Behnke MS, White MW, Striepen B. 2011. A systematic screen to discover and analyze apicoplast proteins identifies a conserved and essential protein import

- factor. *PLoS Pathog* 7:e1002392. <http://dx.doi.org/10.1371/journal.ppat.1002392>.
30. Münter S, Sabass B, Selhuber-Unkel C, Kudryashev M, Hegge S, Engel U, Spatz JP, Matuschewski K, Schwarz US, Frischknecht F. 2009. *Plasmodium* sporozoite motility is modulated by the turnover of discrete adhesion sites. *Cell Host Microbe* 6:551–562. <http://dx.doi.org/10.1016/j.chom.2009.11.007>.
 31. Sebastian S, Brochet M, Collins MO, Schwach F, Jones ML, Goulding D, Rayner JC, Choudhary JS, Billker O. 2012. A *Plasmodium* calcium-dependent protein kinase controls zygote development and transmission by translationally activating repressed mRNAs. *Cell Host Microbe* 12:9–19. <http://dx.doi.org/10.1016/j.chom.2012.05.014>.
 32. Baum J, Papenfuss AT, Baum B, Speed TP, Cowman AF. 2006. Regulation of apicomplexan action-based motility. *Nat Rev Microbiol* 4:621–628. <http://dx.doi.org/10.1038/nrmicro1465>.
 33. Frénal K, Marq J-B, Jacot D, Polonais V, Soldati-Favre D. 2014. Plasticity between MyoC- and MyoA-glideosomes: an example of functional compensation in *Toxoplasma gondii* invasion. *PLoS Pathog* 10:e1004504. <http://dx.doi.org/10.1371/journal.ppat.1004504>.
 34. Franke JD, Bourry AL, Gerald NJ, Kiehart DP. 2006. Native nonmuscle myosin II stability and light chain binding in *Drosophila melanogaster*. *Cell Motil Cytoskeleton* 63:604–622. <http://dx.doi.org/10.1002/cm.20148>.
 35. Weissbach L, Bernardis A, Herion DW. 1998. Binding of myosin essential light chain to the cytoskeleton-associated protein IQGAP1. *Biochem Biophys Res Commun* 251:269–276. <http://dx.doi.org/10.1006/bbrc.1998.9371>.
 36. Lamarque MH, Roques M, Kong-Hap M, Tonkin ML, Rugarabamu G, Marq J-B, Penarete-Vargas DM, Boulanger MJ, Soldati-Favre D, Lebrun M. 2014. Plasticity and redundancy among AMA-RON pairs ensure host cell entry of *Toxoplasma* parasites. *Nat Commun* 5:4098. <http://dx.doi.org/10.1038/ncomms5098>.
 37. Fujita-Becker S, Dürrwang U, Erent M, Clark RJ, Geeves MA, Manstein DJ. 2005. Changes in Mg²⁺ ion concentration and heavy chain phosphorylation regulate the motor activity of a class I myosin. *J Biol Chem* 280:6064–6071. <http://dx.doi.org/10.1074/jbc.M412473200>.
 38. De La Roche MA, Lee S-F, Côté GP. 2003. The *Dictyostelium* class I myosin, MyoD, contains a novel light chain that lacks high-affinity calcium-binding sites. *Biochem J* 374:697–705. <http://dx.doi.org/10.1042/BJ20030656>.
 39. Sweeney HL, Houdusse A. 2010. Structural and functional insights into the myosin motor mechanism. *Annu Rev Biophys* 39:539–557. <http://dx.doi.org/10.1146/annurev.biophys.050708.133751>.
 40. Warshaw DM, Guilford WH, Freyzo Y, Kremntsova E, Palmiter KA, Tyska MJ, Baker JE, Trybus KM. 2000. The light chain binding domain of expressed smooth muscle heavy meromyosin acts as a mechanical lever. *J Biol Chem* 275:37167–37172. <http://dx.doi.org/10.1074/jbc.M006438200>.
 41. Uyeda TQ, Abramson PD, Spudich JA. 1996. The neck region of the myosin motor domain acts as a lever arm to generate movement. *Proc Natl Acad Sci U S A* 93:4459–4464. <http://dx.doi.org/10.1073/pnas.93.9.4459>.
 42. Ni S, Hong F, Haldeman BD, Baker JE, Facemyer KC, Cremo CR. 2012. Modification of interface between regulatory and essential light chains hampers phosphorylation-dependent activation of smooth muscle myosin. *J Biol Chem* 287:22068–22079. <http://dx.doi.org/10.1074/jbc.M112.343491>.
 43. Eswar N, Webb B, Marti-Renom MA, Madhusudhan MS, Eramian D, Shen M-Y, Pieper U, Sali A. 2007. Comparative protein structure modeling using MODELLER. *Curr Protoc Protein Sci Chapter 2:Unit 2.9*.
 44. Pronk S, Páll S, Schulz R, Larsson P, Bjelkmar P, Apostolov R, Shirts MR, Smith JC, Kasson PM, van der Spoel D, Hess B, Lindahl E. 2013. GROMACS 4.5: a high-throughput and highly parallel open source molecular simulation toolkit. *Bioinformatics* 29:845–854. <http://dx.doi.org/10.1093/bioinformatics/btt055>.
 45. Jorgensen WL, Maxwell DS, Tirado-Rives J. 1996. Development and testing of the OPLS all-atom force field on conformational energetics and properties of organic liquids. *J Am Chem Soc* 118:11225–11236. <http://dx.doi.org/10.1021/ja9621760>.
 46. Jorgensen WL, Chandrasekhar J, Madura JD. 1983. Comparison of simple potential function for simulating liquid water. *J Chem Phys* 79:926–935. <http://dx.doi.org/10.1063/1.445869>.
 47. Berendsen HJC, Postma JPM, van Gunsteren WF, DiNola A, Haak JR. 1984. Molecular dynamics with coupling to an external bath. *J Chem Phys* 81:3684. <http://dx.doi.org/10.1063/1.448118>.
 48. Darden T, Perera L, Li L, Pedersen L. 1999. New tricks for modelers from the crystallography toolkit: the particle mesh Ewald algorithm and its use in nucleic acid simulations. *Structure* 7:R55–R60. [http://dx.doi.org/10.1016/S0969-2126\(99\)80033-1](http://dx.doi.org/10.1016/S0969-2126(99)80033-1).
 49. Hess B. 2008. P-LINCS: a parallel linear constraint solver for molecular simulation. *J Chem Theory Comput* 4:116–122. <http://dx.doi.org/10.1021/ct700200b>.
 50. Kumar S, Kumar S, Kumar S, Rosenberg JM, Rosenberg JM, Rosenberg JM, Bouzida D, Bouzida D, Bouzida D. 1992. The weighted histogram analysis method for free-energy calculations on biomolecules. I. The method. *J Comput Chem* 13:1011–1021.
 51. Kafsack BF, Beckers C, Carruthers VB. 2004. Synchronous invasion of host cells by *Toxoplasma gondii*. *Mol Biochem Parasitol* 136:309–311. <http://dx.doi.org/10.1016/j.molbiopara.2004.04.004>.
 52. Mehta S, Sibley LD. 2011. Actin depolymerizing factor controls actin turnover and gliding motility in *Toxoplasma gondii*. *Mol Biol Cell* 22:1290–1299. <http://dx.doi.org/10.1091/mbc.E10-12-0939>.
 53. Buguliskis JS, Brossier F, Shuman J, Sibley LD. 2010. Rhomboid 4 (ROM4) affects the processing of surface adhesins and facilitates host cell invasion by *Toxoplasma gondii*. *PLoS Pathog* 6:e1000858. <http://dx.doi.org/10.1371/journal.ppat.1000858>.
 54. Håkansson S, Morisaki H, Heuser J, Sibley LD. 1999. Time-lapse video microscopy of gliding motility in *Toxoplasma gondii* reveals a novel, biphasic mechanism of cell locomotion. *Mol Biol Cell* 10:3539–3547. <http://dx.doi.org/10.1091/mbc.10.11.3539>.
 55. Baker RT, Catanzariti AM, Karunasekara Y, Soboleva TA, Sharwood R, Whitney S, Board PG. 2005. Using deubiquitylating enzymes as research tools. *Methods Enzymol* 398:540–554.